MATERIALS SCIENCE

# Electronic-grade epitaxial (111) $KTaO_3$ heterostructures

**Jieun Kim[1]†, Muqing Yu[2,3]†, Jung-Woo Lee[1]†, Shun-Li Shang[4], Gi-Yeop Kim[5], Pratap Pal[1], Jinsol Seo[6,7], Neil Campbell[8], Kitae Eom[1], Ranjani Ramachandran[2,3], Mark S. Rzchowski[8], Sang Ho Oh[6,7], Si-Young Choi[5], Zi-Kui Liu[4], Jeremy Levy[2,3], Chang-Beom Eom[1]***



**$KTaO_3$ heterostructures have recently attracted attention as model systems to study the interplay of quantum paraelectricity, spin-orbit coupling, and superconductivity. However, the high and low vapor pressures of potassium and tantalum present processing challenges to creating heterostructure interfaces clean enough to reveal the intrinsic quantum properties. Here, we report superconducting heterostructures based on high-quality epitaxial (111) $KTaO_3$ thin films using an adsorption-controlled hybrid PLD to overcome the vapor pressure mismatch. Electrical and structural characterizations reveal that the higher-quality heterostructure interface between amorphous $LaAlO_3$ and $KTaO_3$ thin films supports a two-dimensional electron gas with substantially higher electron mobility, superconducting transition temperature, and critical current density than that in bulk single-crystal $KTaO_3$-based heterostructures. Our hybrid approach may enable epitaxial growth of other alkali metal–based oxides that lie beyond the capabilities of conventional methods.**

## INTRODUCTION

Quantum materials made of transition metal oxides display numerous interesting physical properties such as magnetism, ferroelectricity, interfacial conductivity, and superconductivity (*1*–*5*). In their epitaxial thin-film forms, the strong *d* electron correlations that determine many of their physical properties can be easily manipulated through coupling to strain, dimensionality, and chemical pressures (*6*–*8*). Traditionally, pulsed-laser deposition (PLD) and molecular-beam epitaxy (MBE) have been workhorse synthesis tools in the quest to produce a model thin-film version of novel quantum materials exhibiting exotic quantum phenomena (*9*–*11*). In PLD, a target having the desired composition as the growing film is ablated by a pulsed-laser beam, creating a plume consisting of a stoichiometric mixture of high-energetic ions. In contrast, MBE thermally evaporates each element from separate effusion cells, creating a low-energy molecular beam of evaporated atoms. Although both are excellent techniques with wide-ranging applications, and with numerous interesting materials synthesized (*12*–*14*) including $A^{1+}B^{5+}O_3$ perovskite oxides (*15*, *16*) and even rubidium-containing compounds (*17*), the synthesis of (111)-oriented potassium tantalate ($KTaO_3$) presents distinct challenges for either MBE or PLD alone. First, the extremely large vapor pressure mismatch of constituent species (fig. S1) presents considerable processing challenges for growing atomically precise and stoichiometric thin films. To alleviate these issues, approaches such as potassium-enriched ablation targets (*18*) in PLD and suboxide tantalum sources (*19*) in MBE have been put forth. Second, the high energy of the particularly interesting and useful (111) surface makes epitaxial growth notoriously difficult (*20*), with films prone to nanoscale faceting. Although a combination of reduced substrate temperatures and highly energetic techniques (e.g., PLD and sputtering) can lead to smooth epitaxial films (*21*), the resulting films usually contain a high concentration of point defects. So far, only limited examples of successful growth of (111)-oriented perovskite films are reported using low-energy deposition techniques such as MBE (*22*, *23*).

Here, we describe an alternative approach to (111) $KTaO_3$, hybrid PLD, which synergistically combines the advantages of PLD and MBE (*24*). Here, we supply K by thermal evaporation of a $K_2O$ effusion cell as in MBE, and Ta by ablating a ceramic target of tantalum pentoxide ($Ta_2O_5$) with a pulsed excimer laser as in PLD, to produce adsorption-controlled epitaxial growth. We synthesize high-quality epitaxial thin films of (111)-oriented $KTaO_3$ and analyze superconducting two-dimensional electron gases (2DEGs) at its interface with $LaAlO_3$. $KTaO_3$ on its own hosts many interesting physical properties such as quantum paraelectricity and large spin-orbit coupling (*25*–*27*). Bulk single-crystal $KTaO_3$ (111)-based heterointerfaces including EuO/$KTaO_3$ (111) (*4*), $LaTiO_3$/$KTaO_3$ (111) (*28*), $La_{2/3}Sr_{1/3}MnO_3$/$KTaO_3$ (111) (*29*), $AlO_x$/$KTaO_3$ (111) (*30*), and $LaAlO_3$/$KTaO_3$ (111) (*5*) have displayed superconductivity with a high superconducting transition temperature ($T_c$) ≈ 1 to 2 K, and with properties inherently correlated with the crystallographic orientation (*31*). Reducing the point defect concentrations below that of bulk single crystals is a key challenge for studying the origin of this superconductivity and related quantum phenomena (*27*) such as ferroelectric quantum criticality (*32*–*34*), topological superconductivity (*35*), and superconducting spintronics (*36*). Using a combination of thermodynamic analysis (*37*) and synthesis design (*38*), we are able to grow high-quality homoepitaxial $KTaO_3$ thin films on buffered single-crystal $KTaO_3$ (111) substrates, followed by an in situ $LaAlO_3$ growth with conventional PLD.

## RESULTS

### Adsorption-controlled hybrid synthesis approach

To predict the growth parameters of a stoichiometric $KTaO_3$ phase in hybrid PLD, we built a thermodynamic database for the K-Ta-O

[1]Department of Materials Science and Engineering, University of Wisconsin-Madison, Madison, WI 53706, USA. [2]Department of Physics and Astronomy, University of Pittsburgh, Pittsburgh, PA 15260, USA. [3]Pittsburgh Quantum Institute, Pittsburgh, PA 15260, USA. [4]Department of Materials Science and Engineering, The Pennsylvania State University, University Park, PA 16802, USA. [5]Department of Materials Science and Engineering, Pohang University of Science and Technology, 77 Cheongam-Ro, Pohang 37673, Republic of Korea. [6]Department of Energy Science, Sungkyunkwan University, Suwon 16419, Korea. [7]Department of Energy Engineering, KENTECH Institute for Energy Materials and Devices, Korea Institute of Energy Technology (KENTECH), Naju 58330, Republic of Korea. [8]Department of Physics, University of Wisconsin-Madison, Madison, WI 53706, USA.
*Corresponding author. Email: ceom@wisc.edu
†These authors contributed equally to this work.

system (*39*) and predicted relevant phase diagrams (figs. S2 to S4). Figure 1A shows the calculated stability phase diagram of K-Ta-O near the stoichiometric $KTaO_3$ as a function of K partial pressure and temperature (see fig. S3 for a complete phase diagram of Fig. 1A); here, the oxygen ($O_2$) partial pressure is fixed at $10^{-6}$ torr based on the potential phase diagram as a function of K and $O_2$ partial pressures (fig. S4). In our synthesis, we used commercially available potassium oxide ($K_2O$) as K source because elemental K is extremely unstable in both the ambient and high temperature/vacuum conditions (*39*). We estimate the source temperatures for achieving stoichiometric $KTaO_3$ synthesis by calculating partial pressures of all gas species (Fig. 1B) at source temperatures from 500 to 1000 K. We identify three major gas species as $O_2$, $K_2O_2$, and K with the calculated equilibrium partial pressures $\approx 1.7 \times 10^{-3}$, $9.2 \times 10^{-7}$, and $3.9 \times 10^{-7}$ torr, respectively, at a source temperature of 750 K. These values set the upper limits for the partial pressures of gas species.

In our experiments, the vacuum chamber is constantly evacuated, maintaining dynamic equilibrium, so that the total dynamic pressure from the combined gas phases at a source temperature of 750 K comes to $\approx 10^{-6}$ torr (*39*). The chamber pressure was kept well below $10^{-3}$ torr to maintain the molecular flow state of gas species and sufficient overpressure of potassium near the substrate surface. These analyses indicated that the practical growth window of $KTaO_3$ should be in the range of $10^{-7}$ to $10^{-9}$ torr K partial pressure and 950 to 1000 K substrate temperatures (red box, Fig. 1A). Figure 1C schematically depicts the hybrid PLD experimental setup (*39*). As with MBE, K is supplied by thermal evaporation of a $K_2O$ effusion cell directed at the substrate. In contrast, Ta is supplied by ablating a ceramic target of tantalum pentoxide ($Ta_2O_5$) with a pulsed excimer laser as in PLD. Figure 1D schematically illustrates the adsorption-controlled growth of $KTaO_3$. In adsorption-controlled growth (*40*), the volatile species (K in this case) is provided with sufficiently large overpressure to avoid K deficiency, while excess K readily evaporates from the K-terminated surface. Although $KTaO_3$ melts incongruently (*41*) and hence perfect stoichiometry may still be challenging, the proximity to thermodynamic equilibrium afforded by the adsorption-controlled growth minimizes unintentional defects and hence facilitates the synthesis of high-quality $KTaO_3$ thin films.

## Epitaxial thin-film synthesis

We grew ≈8- to 10-nm-thick epitaxial $KTaO_3$ thin films on single-crystal substrates of $SrTiO_3$ (001), $SrTiO_3$ (111), and $KTaO_3$ (111) and on $KTaO_3$ (111) with an ≈1-nm-thick $SmScO_3$ template layer (figs. S5 to S7). In the main text, we only discuss the films grown homoepitaxially on $KTaO_3$ (111) for brevity. Homoepitaxial $KTaO_3$ thin films grown directly on bare $KTaO_3$ (111) substrates at 973 K substrate temperature show atomically smooth surfaces (fig. S7B), but x-ray diffraction indicates a slight off-stoichiometry of the $KTaO_3$ thin film (fig. S7H). An increased substrate temperature of 1023 K enhances stoichiometry but results in surface roughening generating the more thermodynamically stable (001) and (011) facets (fig. S7C) (*20*, *22*). To address these issues, we grew a thin $SmScO_3$ template on $KTaO_3$ (111) substrates and grew stoichiometric and smooth $KTaO_3$ thin films at low substrate temperature. The



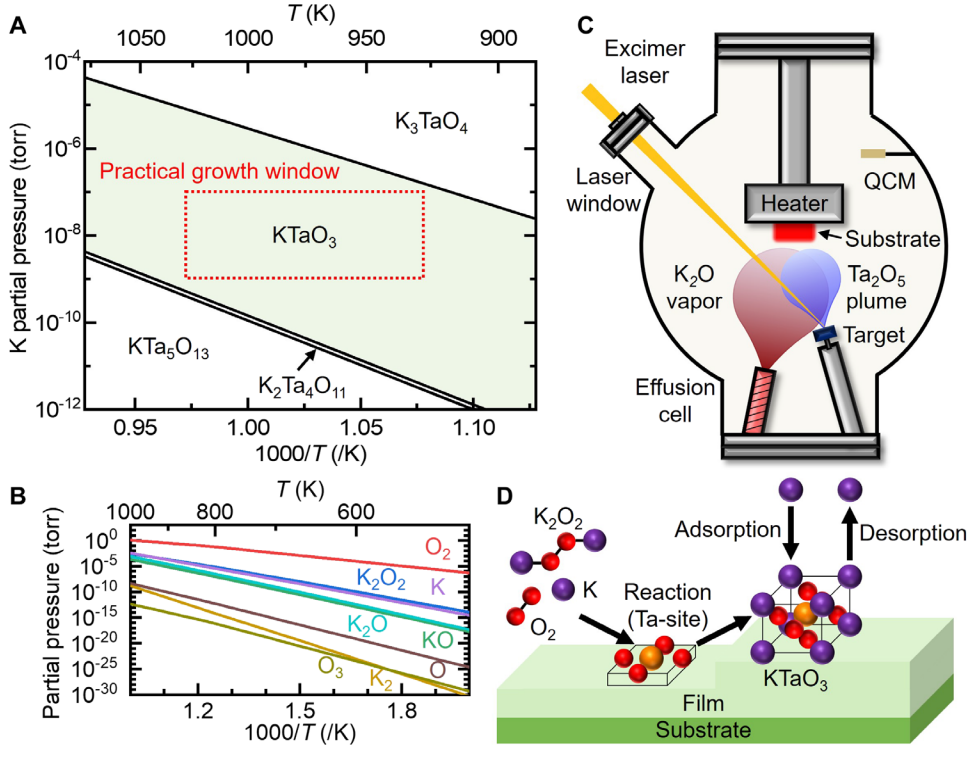


**Fig. 1. Thermodynamics-guided epitaxial growth of $KTaO_3$ thin films by hybrid PLD.** (**A**) Phase region of $KTaO_3$ as a function of K partial pressure and temperature at fixed $O_2$ partial pressure of $10^{-6}$ torr. Practical experimental parameters within the $KTaO_3$ growth window are marked by a red box. (**B**) Vapor pressure of gas species in the K-O system. (**C**) Schematic illustrating the hybrid PLD method for $KTaO_3$ thin-film growth. QCM, quartz crystal microbalance. (**D**) Schematic illustrating the adsorption-controlled growth of $KTaO_3$ thin films.

$SmScO_3$ template serves three purposes: (i) stabilizing the $KTaO_3$ surface by suppressing K evaporation from the $KTaO_3$ substrate surface at high temperature and high vacuum (*28*), (ii) inhibiting the migration of native defects from the $KTaO_3$ substrate to the film (*42*) that may deteriorate the superconductivity (fig. S8), and (iii) suppressing the transfer of charge carriers from the film to the substrate area (*43*) where more disorder is expected (*5*, *44*) (fig. S9). To alleviate the lattice parameter and oxygen octahedral rotation mismatch between $SmScO_3$ (space group: *Pbnm*) (*45*) and $KTaO_3$ (space group: $Pm\bar{3}m$) (*46*), we restricted the thickness of $SmScO_3$ template to be ≈1 nm. X-ray diffraction and atomic force microscopy validate this heterostructure design and indicate that the (pseudo-)homoepitaxial $KTaO_3$ thin film grown on $SmScO_3$-buffered $KTaO_3$ (111) substrate is stoichiometric and atomically smooth (fig. S7, D to H).

We characterized the interfacial structures of the $LaAlO_3/KTaO_3/SmScO_3/KTaO_3$ (111) heterostructures using scanning transmission electron microscopy (STEM) (*39*). High-angle annular dark field (HAADF) cross-sectional images of the heterostructures (Fig. 2, A, C, and D) confirm atomically sharp interfaces of $SmScO_3/KTaO_3$ (111) substrate (Fig. 2C) and $LaAlO_3/KTaO_3$ (111) thin film (Fig. 2D), which means that the thin $SmScO_3$ template could protect the unstable (111) surface of the $KTaO_3$ substrate (*28*) under the highly reducing atmosphere of $\approx 10^{-6}$ torr at 973 K. The $KTaO_3$ thin film is fully epitaxial to the $KTaO_3$ substrate through the underlying $SmScO_3$ template without any misfit dislocations, facilitated by the small 2.6% lattice mismatch between $SmScO_3$ and $KTaO_3$ (111). The crystal structure of ≈1-nm-thick $SmScO_3$ film appears to adopt a (pseudo-)cubic structure, as can be seen in the alignment of Sm columns along the [001] direction without a buckling angle (fig. S10). This allows the $KTaO_3$ (111) thin film to be coherently grown with the desired cubic structure due to the (pseudo-)cubic $SmScO_3$ template. The STEM image of Fig. 2A shows a contrast variation near the $LaAlO_3/KTaO_3$ (111) thin film and $SmScO_3/KTaO_3$ (111) substrate interfaces. We attribute the brighter contrast in the $KTaO_3$ (111) thin

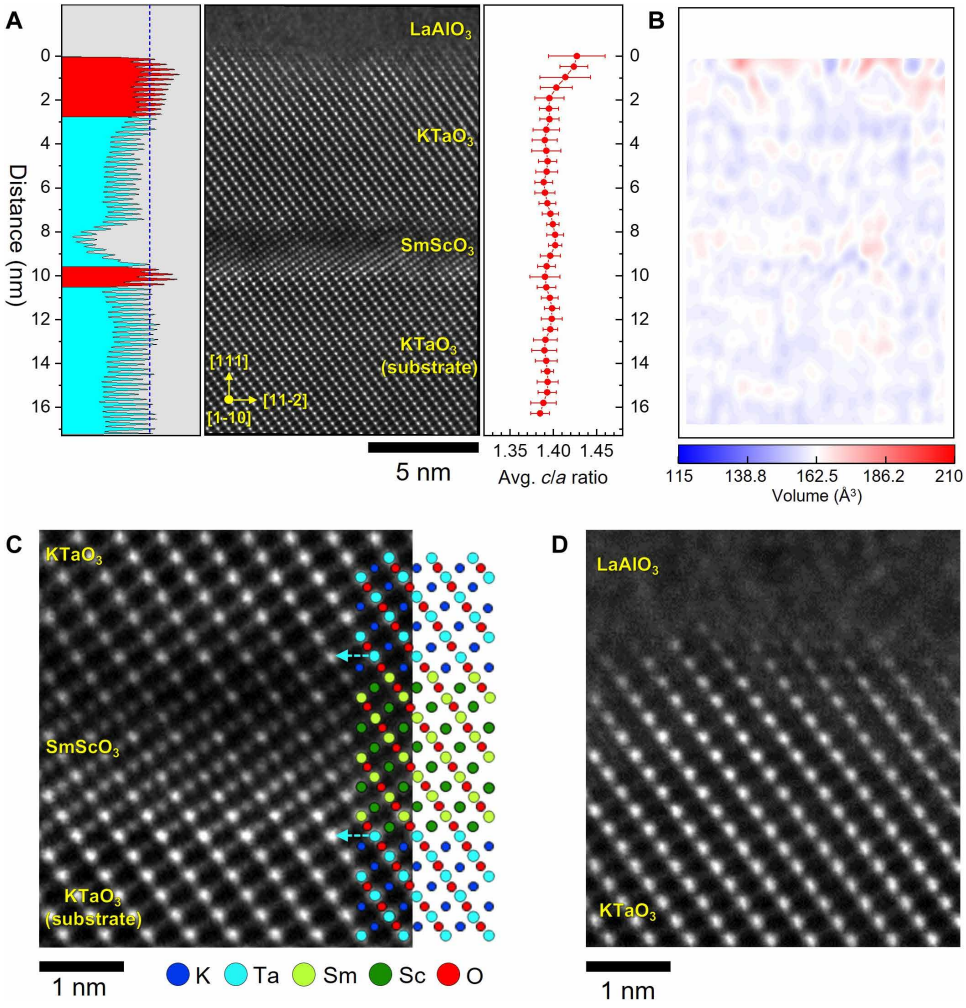


**Fig. 2. Atomically sharp interfaces in epitaxial $LaAlO_3/KTaO_3/SmScO_3/KTaO_3$ (111) heterostructure.** (**A**) HAADF-STEM image of cross section viewed along the [1-10] and intensity profile. Red color in the intensity profile indicates the regions appearing brighter in the image near the interfaces of $LaAlO_3/KTaO_3$ thin film and $SmScO_3/KTaO_3$ substrate. (**B**) Volume color mapping and average volume measurement in (A). The average volume is close to the ideal volume in a cubic structure. Approximately ≈2-nm-thick regions of higher volume are observed near the $LaAlO_3/KTaO_3$ thin-film interface, indicating that the oxygen vacancies are confined to the top of the $LaAlO_3/KTaO_3$ thin-film interface. (**C**) Magnified image of the $KTaO_3$ thin film/$SmScO_3/KTaO_3$ substrate region. (**D**) Magnified image of the $LaAlO_3/KTaO_3$ thin-film region.

film near the top interface of $LaAlO_3/KTaO_3$ (111) thin film to the presence of doubly charged oxygen vacancies ($V_O^{\cdot\cdot}$), which are predicted to increase the Ta-O and decrease the K-O bond lengths by ≈1.66% (*46*). This corresponds to expansion along the out-of-plane direction and increase of *c*/*a* and cell volume (Fig. 2, A and B). We attribute the brighter contrast in the $KTaO_3$ (111) substrate near the bottom $SmScO_3/KTaO_3$ (111) substrate interface to singly charged K vacancies ($V_K'$), which have a lower formation energy of ≈0.06 eV than $V_O^{\cdot\cdot}$ (≈0.18 eV) and do not change the cell dimension (*46*). These observations directly confirm the higher crystalline quality of the $KTaO_3$ (111) thin film compared to the $KTaO_3$ (111) bulk single-crystal substrate.

## High-quality epitaxial (111) $KTaO_3$ heterostructures

These lower defect concentrations improve both the normal state and superconducting state properties of 2DEG at the $LaAlO_3/KTaO_3$ interface. We first compare normal-state transport measurements of two different heterostructures: $LaAlO_3/KTaO_3$ (111) substrate (denoted as "Bulk" and $LaAlO_3/KTaO_3/SmScO_3/KTaO_3$ (111) substrate (denoted as "Film") (Fig. 3) (*39*). In both cases, the $LaAlO_3$ growth was carried out by conventional PLD at a heater temperature of 673 K in a dynamic oxygen pressure of $10^{-5}$ torr with a laser fluence of 1.6 J/cm$^2$ and a laser repetition rate of 1 Hz from a single-crystal $LaAlO_3$ target (*39*). In the case of Film, $LaAlO_3$ was grown in situ after $KTaO_3$ growth and post-annealing. Consistent with the literature (*5*), $LaAlO_3$ grows with an amorphous structure (Fig. 2A). As shown in Fig. 3A, 2DEGs are created at the $LaAlO_3/KTaO_3$ interface. The amorphous $LaAlO_3$ layer is grown in situ in the case of $LaAlO_3/KTaO_3/SmScO_3/KTaO_3$ (111) heterostructures to produce clean $LaAlO_3/KTaO_3$ interface (*47*). Normal state transport data (2 K < *T* < 300 K) were obtained with a van der Pauw geometry that probes the entire sample surface (Materials and Methods). Figure 3B shows the $R_{sq}$-*T* data of the Bulk and Film samples. The Film sample shows much lower $R_{sq}$ in the normal state (Fig. 3B) despite having nearly the same $n_{2D}$ as the Bulk sample at 10 K (Fig. 3C). We attribute the lower $R_{sq}$ to the high carrier mobility (μ) of the Film sample (≈150 cm$^2$/Vs at 10 K) compared to the Bulk sample (≈48 cm$^2$/Vs at 10 K) (Fig. 3D). We tested multiple samples with similar structure, and summarize their properties at 10 K in a μ-$n_{2D}$ diagram (Fig. 3E). This demonstrates that the $LaAlO_3/KTaO_3/SmScO_3/KTaO_3$ (111) (red up-triangles, Fig. 3E) samples generally have higher μ within the same $n_{2D}$ range compared to the $LaAlO_3/KTaO_3$ (111) samples (black down-triangles, Fig. 3E). We attribute the differences in μ to the lower point defect concentrations, which control the low-temperature mobility. To further confirm the superior quality of the $LaAlO_3/KTaO_3/SmScO_3/KTaO_3$ (111) samples, we analyzed the $n_{2D}$ dependence of the mean free path (*l*) and Ioffe-Regel parameter $k_F l$ at 10 K, with $k_F$ the Fermi wave vector (figs. S11 and S12) (*39*). This confirms that the $LaAlO_3/KTaO_3/SmScO_3/KTaO_3$ (111) samples also have higher *l* and $k_F l$ than the $LaAlO_3/KTaO_3$ (111) samples and those reported in the literature (*4*, *5*) regardless of $n_{2D}$. Our analyses presented so far—x-ray diffraction, atomic force microscopy, STEM, and electrical transport measurements—cement hybrid PLD as an effective synthesis method producing electronic-grade $KTaO_3$ thin films much cleaner than their bulk single-crystal counterparts.

## Superconductivity

We patterned Hall bars along [11-2] and [1-10] on the Bulk and Film samples to investigate the superconductivity in $KTaO_3$ (Fig. 4A) (*39*). In the main text, we focus on electrical transport. Additional data on the Berezinskii-Kosterlitz-Thouless (BKT) transitions (fig. S13) and magnetotransport (figs. S14 to S16) are provided. Figure 4A shows the $R_{sq}$ versus *T* data at *T* < 2 K along [11-2]. The Film sample shows $T_c \approx 1.5$ K, which is 25% higher than the $T_c \approx 1.2$ K exhibited by the



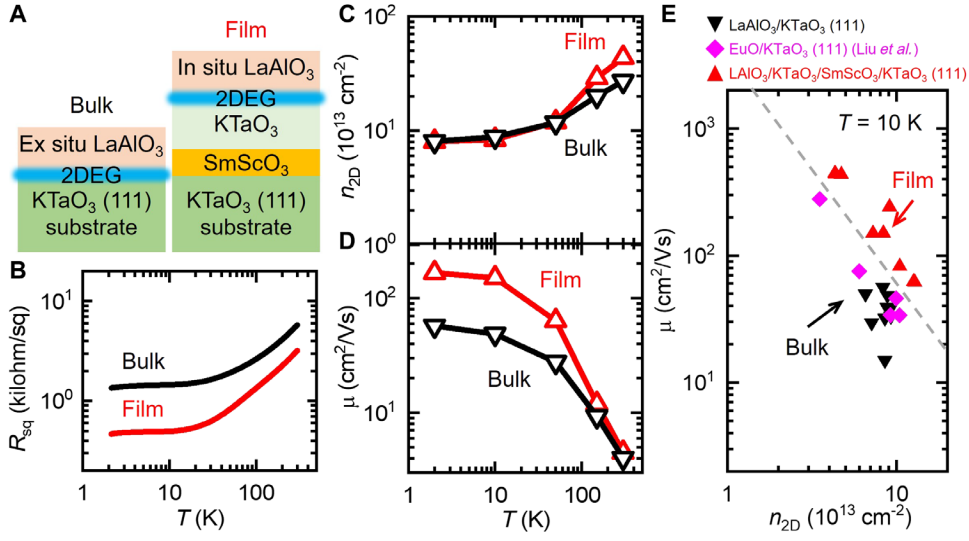


**Fig. 3. Electrical transport measurements of $KTaO_3$ (111).** (**A**) Schematic illustrating the structures of the measured samples. In the bulk case, the $LaAlO_3$ overlayer is always grown ex situ, which inevitably creates 2DEG in the first few nanometers of $KTaO_3$ with high defect density. In the case of $KTaO_3$ thin film, the $LaAlO_3$ layer is grown in situ and the surface of $KTaO_3$ has low defect density, which results in enhanced μ. (**B** to **D**), Temperature dependence (2 to 300 K) of (B) $R_{sq}$, (C) $n_{2D}$, and (D) μ of $LaAlO_3/KTaO_3$ (111) (Bulk) and $LaAlO_3/KTaO_3/SmScO_3/KTaO_3$ (111) (Film) heterostructures. The measurements in (B) to (D) are performed in a van der Pauw geometry. (**E**) Distribution of μ and $n_{2D}$ estimated from Hall measurements at *T* = 10 K. The samples shown in (B) to (D) are marked with arrows. Purple diamonds are data at *T* = 10 K from different growth conditions of EuO from Liu *et al.* (*4*).

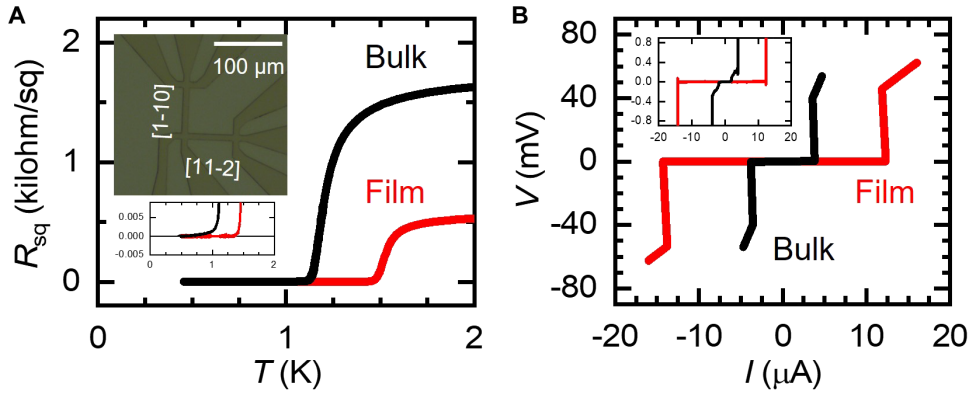


**Fig. 4. Superconductivity of $KTaO_3$ (111).** (**A**) Temperature dependence of $R_{sq}$ along the [11-2] on Hall bars. The insets show an optical micrograph of Hall bars (top) and a magnified view near the transition (bottom). (**B**) *V-I* curves along the [11-2] measured at $T = 0.5$ K on Hall bars. The inset shows a magnified view near the transition.

Bulk sample. The *V-I* curves at $T = 0.5$ K (Fig. 4B) confirm the enhanced superconductivity in the Film sample with a critical current $I_c$ (≈12.3 μA), substantially larger than $I_c$ of the Bulk sample (≈3.9 μA) with a similar $n_{2D}$. The $R_{sq}$-$T$, *V-I* data (Fig. 4 and figs. S17 to S19) suggest that reduced disorder (i.e., higher μ) eliminates signatures of disorder-induced inhomogeneities (*48*) observed in the superconductivity of $KTaO_3$ (111) such as anisotropic transport (*4*), residual resistance (*5*), and step-like *V-I* curves (figs. S18 and S19), which appear to be highly sensitive to μ (*5*).

## DISCUSSION

We have synthesized high-quality $KTaO_3$ heterostructures with hybrid PLD and demonstrated that the increased quality leads to superior low-temperature mobility and superconducting properties of the interfacial 2DEGs that they support. The ability of hybrid PLD to overcome vapor pressure mismatch roadblocks to grow high-quality thin films has enabled synthesis of $KTaO_3$ with disorder reduced enough to allow insight into the intrinsic properties of $KTaO_3$ (111) interfaces and their dependence on carrier density (fig. S20), stoichiometry (fig. S22), and disorder (figs. S12, S17, and S18). It also opens the door to exploring the untapped potential of many unexplored thin-film systems and derivative heterostructures such as freestanding membranes (*49*). Beyond $KTaO_3$, a synthesis method of compounds containing both highly volatile and refractory elements in thin-film form holds promise for revolutionizing a wide range of technologies, including environment-friendly microelectromechanical systems (*50*), integrated solid-state batteries (*51*), and emerging quantum technologies (*27*, *52*).

## MATERIALS AND METHODS

### Thermodynamic calculations of the K-Ta-O system

The thermodynamic database used in the present work is based on the SGTE substance database (i.e., the SSUB5) (*53*). However, thermodynamic properties for the six ternary oxides ($KTa_5O_{13}$, $K_2Ta_4O_{11}$, $KTaO_3$, $K_3TaO_4$, $K_3Ta_8O_{21}$, and $K_2Ta_{15}O_{32}$) are absent in SSUB5. Here, their thermodynamic properties are estimated with the reference states being the binary oxides (and pure element Ta) in SSUB5 according to the reactions in table S1. The reaction enthalpies $\Delta H$ for these ternary oxides are based on density functional theory (DFT)–based first-principles calculations in the literature, i.e., the Materials Project (MP) (*54*) and the Open Quantum Materials Database (OQMD) (*55*); see the predicted $\Delta H$ values in table S1. Using the presently generated K-Ta-O database (SSUB5 together with the DFT-based $\Delta H$ values), we perform thermodynamic calculations using the Thermo-Calc software (*56*).

### Film synthesis and structural characterizations

Hybrid PLD using a KrF excimer laser (248 nm, LPX 300, Coherent) and a homebuilt effusion cell were used to grow epitaxial $KTaO_3$ thin films on single-crystal $KTaO_3$ (111), $SrTiO_3$ (111), and $SrTiO_3$ (001) substrates. To obtain the $TiO_2$-terminated substrates, as-received $SrTiO_3$ substrates were etched using buffered hydrofluoric acid (Sigma-Aldrich) for 1 min and annealed at 1273 K for 6 hours. The $KTaO_3$ growth was carried out at a substrate heater temperature of 973 K in a chamber pressure of $10^{-5}$ torr using argon as background gas. To supply tantalum, a ceramic target of $Ta_2O_5$ (purity 99.9%, Praxair) was ablated using a laser fluence of 0.5 J/cm$^2$ and a laser repetition rate of 20 Hz with a target-to-substrate distance of 65 mm. To supply potassium, 5 g of $K_2O$ powders (purity 99.9%, Nanoshel) was used as source and loaded in a cylindrical magnesium oxide crucible with a diameter of 16 mm and a length of 100 mm. To protect the effusion cell from reaction with potassium vapors, the effusion cell was shielded with tantalum foils. The crucible was heated using a homebuilt effusion cell, and $K_2O$ source was pre-evaporated at an effusion cell temperature of 873 K in vacuum for de-gassing. Following pre-evaporation, the effusion cell temperature was lowered to 750 K and maintained during the $KTaO_3$ growth. Following the $KTaO_3$ growth, the samples were cooled to 823 K by quenching in a static oxygen pressure of 500 torr and annealed in situ for 30 min. The growth rate for $KTaO_3$ was approximately 0.0044 Å per laser pulse (≈2.5 unit cell/min). The laser fluence was kept at slightly above the ablation threshold for $Ta_2O_5$ ceramic to minimize the high kinetic energy ion bombardment during the $KTaO_3$ growth. The $SmScO_3$ growth was carried out by conventional PLD at a heater temperature of 973 K in a dynamic oxygen pressure of 20 mtorr with a laser fluence of 0.9 J/cm$^2$ and a laser repetition rate of 1 Hz from a ceramic target (Praxair) of the same composition with a target-to-substrate distance of 65 mm. The growth rate of $SmScO_3$ was approximately 0.066 Å per laser pulse. Following the growth, the samples were cooled to room temperature by quenching in a static oxygen pressure

of 500 torr. The $LaAlO_3$ growth was carried out in situ by conventional PLD at a heater temperature of 673 K in a dynamic oxygen pressure of $10^{-5}$ torr with a laser fluence of 1.6 J/cm$^2$ and a laser repetition rate of 1 Hz from a single-crystal $LaAlO_3$ target (Crystec) with a target-to-substrate distance of 65 mm. The growth rate of $LaAlO_3$ was approximately 0.11 Å per laser pulse. Following the growth, the samples were cooled to room temperature by quenching in the growth atmosphere. X-ray diffraction measurements were conducted with a high-resolution x-ray diffractometer (Bruker). Surface topography images were collected with an atomic force microscope operated in a tapping mode (Veeco).

### Scanning transmission electron microscopy

A companion sample to "Film_2" was used for STEM analysis. Transport measurements on the sample for STEM analysis were performed to ensure the sample had representative characteristics. The cross-sectional STEM sample having [1-10] projection was prepared using a dual-beam focused ion beam system (Helios G3, FEI) to observe the interfacial structure. A thin specimen was prepared using a Ga ion beam at 30 kV with different acceleration voltages from 5 to 1 kV for the sample cleaning process to minimize the damage from Ga ions. The atomic structure was investigated using a STEM (JEM-ARM200F, JEOL, Japan) operating at 200 kV equipped with a fifth-order probe corrector (ASCOR, CEOS GmbH, Germany) at Materials Imaging & Analysis Center of POSTECH in South Korea. The optimal size of the electron probe for STEM observation was ~78 pm. The collection semi-angles of the HAADF detector were adjusted from 68 to 280 mrad to collect scattered electrons in a large angle to obtain clear Z-sensitive images. HAADF-STEM imaging was performed using Smart Align (HREM Research Inc., Japan), which conducted the multi-stack of images and aligned them using rigid registration to correct the sample drift and scan distortions. The obtained raw images were processed using a band-pass difference filter with a local window to reduce background noise (Filters Pro, HREM Research Inc., Japan). HAADF-STEM image analysis was performed by Python with the customized atomic analysis code. All atomic coordinates were determined by the centroid of each atomic column. *c/a* ratio and volume mapping were conducted by the nearest Ta sites of $KTaO_3$ or Sm sites of $SmScO_3$ along the [111] of *c* and [11-2] of *a* directions.

### Device fabrication

Hall bars were fabricated with standard photolithography. First, Au markers were deposited for alignment purpose. AZ4210 photoresist was patterned to cover and protect the Hall bar-shaped regions. The exposed regions underwent inductively coupled plasma reactive ion etching (ICPRIE) for 18 min in a Plasma-Therm APEX ICPRIE. During the etching, 5 sccm (standard cubic centimeters per minute) of $BCl_3$, 50 sccm of $Cl_2$, and 5 sccm of Ar were used as gas etchant, with RIE power set to 100 W. After the etching, photoresist was removed in MICROPOSIT Remover 1165 and then acetone and isopropyl alcohol. The etching depth is measured to be ≈50 nm with an atomic force microscope.

### Electrical transport

The electrical transport measurements were carried out using a four-contact van der Pauw geometry over a temperature range of 2 to 300 K. Two van der Pauw sheet resistance configurations and two Hall measurement configurations were switched between while sweeping a magnetic field over a range of −1 to 1 T. Individual configuration resistances were computed by sourcing a DC of alternating polarity and combining the voltages to compute a resistance free of voltage noise from effects including the Seebeck effect. The two resistances from the sheet-resistance configurations ($R_1$, $R_2$) were combined using the van der Pauw equation, $1 = \exp(-\pi R_1/R_{sq}) + \exp(-\pi R_2/R_{sq})$, to determine the sheet resistance, $R_{sq}$. The two Hall resistances were averaged to compute the Hall resistance, $R_H$. The carrier density, $n_{2D}$, was computed with the equation $n_{2D} = 1/[(dR_H/dB)q]$, where $I$ is the magnitude of the DC sourced and $q$ is the electron charge. The mobility, μ, was computed with the equation $\mu = 1/(R_{sq}\, n_{2D}\, q)$. $k_F$ and $l$ were computed with the equations $k_F = (2\pi n_s)^{1/2}$ and $l = h/(e^2 k_F R_{sq})$.

### Magnetotransport and superconductivity

Superconductivity measurements on Hall bars below 2 K were carried out in a Quantum Design PPMS refrigerator with a dilution unit. Source voltages were applied by a 24-bit digital/analog converter National Instruments PXI-4461, which can also simultaneously perform 24-bit analog/digital conversion. Current biasing was achieved with a 300-kilohm resistor in series with the Hall bar device. The drain current and voltages were measured after amplification by a Krohn-Hite Model 7008 Multi-channel Pre-amplifier. For each current-voltage characteristic, the current sweep started from 0 bias, then went to maximum bias, to minimum bias, and finally finished at 0 bias. The whole sweep took ≈20 s. For 0 bias resistance measurement, a small AC current $I = I_0\cos(2\pi\, ft)$ was sourced where $f = 13$ Hz and $I_0 < 100$ nA. The voltage $V_0$ across the Hallbar channel was measured by a homemade digital lock-in amplifier to get four-terminal resistance $R = V_0/I_0$. High-field magnetoresistance measurements on Hall bars were performed in a Leiden MNK dilution fridge equipped with an Oxford 18T magnet.

## Supplementary Materials

**This PDF file includes:**

Supplementary Text
Figs. S1 to S22
Tables S1 and S2
References

## REFERENCES AND NOTES


1. H. Y. Hwang, Y. Iwasa, M. Kawasaki, B. Keimer, N. Nagaosa, Y. Tokura, Emergent phenomena at oxide interfaces. *Nat. Mater.* **11**, 103–113 (2012).
2. J. Manhart, D. G. Schlom, Oxide interfaces—An opportunity for electronics. *Science* **327**, 1607–1611 (2010).
3. K. Ueno, S. Nakamura, H. Shimotani, H. T. Yuan, N. Kimura, T. Nojima, H. Aoki, Y. Iwasa, M. Kawasaki, Discovery of superconductivity in $KTaO_3$ by electrostatic carrier doping. *Nat. Nanotechnol.* **6**, 408–412 (2011).
4. C. Liu, X. Yan, D. Jin, Y. Ma, H.-W. Hsiao, Y. Lin, T. M. Bretz-Sullivan, X. Zhou, J. Pearson, B. Fisher, J. S. Jiang, W. Han, J.-M. Zuo, J. Wen, D. D. Fong, J. Sun, H. Zhou, A. Bhattacharya, Two-dimensional superconductivity and anisotropic transport at $KTaO_3$ (111) interfaces. *Science* **371**, 716–721 (2021).
5. Z. Chen, Y. Liu, H. Zhang, Z. Liu, H. Tian, Y. Sun, M. Zhang, Y. Zhou, J. Sun, Y. Xie, Electric field control of superconductivity at the $LaAlO_3/KTaO_3$ (111) interface. *Science* **372**, 721–724 (2021).
6. N. M. Dawley, E. J. Marksz, A. M. Hagerstrom, G. H. Olsen, M. E. Holtz, V. Goian, C. Kadlec, J. Zhang, X. Lu, J. A. Drisko, R. Uecker, S. Ganschow, C. J. Long, J. C. Booth, S. Kamba, C. J. Fennie, D. A. Muller, N. D. Orloff, D. G. Schlom, Targeted chemical pressure yields tuneable millimetre-wave dielectric. *Nat. Mater.* **19**, 176–181 (2020).
7. A. K. Yadav, C. T. Nelson, S. L. Hsu, Z. Hong, J. D. Clarkson, C. M. Schlepütz, C. M. Schlepüetz, A. R. Damodaran, P. Shafer, E. Arenholz, L. R. Dedon, D. Chen,

A. Vishwanath, A. M. Minor, L. Q. Chen, J. F. Scott, L. W. Martin, R. Ramesh, Observation of polar vortices in oxide superlattices. *Nature* **530**, 198–201 (2016).
8. K. Choi, M. Biegalski, Y. Li, A. Sharan, J. Schubert, R. Uecker, P. Reiche, Y. Chen, X. Pan, V. Gopalan, L.-Q. Chen, D. Schlom, C. Eom, Enhancement of ferroelectricity in strained $BaTiO_3$ thin films. *Science* **306**, 1005–1009 (2004).
9. G. A. Pan, D. F. Segedin, H. LaBollita, Q. Song, E. M. Nica, B. H. Goodge, A. T. Pierce, S. Doyle, S. Novakov, D. C. Carrizales, A. T. N'Diaye, P. Shafer, H. Paik, J. T. Heron, J. A. Mason, A. Yacoby, L. F. Kourkoutis, O. Erten, C. M. Brooks, A. S. Botana, J. A. Mundy, Superconductivity in a quintuple-layer square-planar nickelate. *Nat. Mater.* **21**, 160–164 (2022).
10. D. Li, K. Lee, B. Y. Wang, M. Osada, S. Crossley, H. R. Lee, Y. Cui, Y. Hikita, H. Y. Hwang, Superconductivity in an infinite-layer nickelate. *Nature* **572**, 624–627 (2019).
11. A. D. Caviglia, S. Gariglio, N. Reyren, D. Jaccard, T. Schneider, M. Gabay, S. Thiel, G. Hammerl, J. Mannhart, J.-M. Triscone, Electric field control of the $LaAlO_3/SrTiO_3$ interface ground state. *Nature* **456**, 624–627 (2008).
12. M. Brahlek, A. S. Gupta, J. Lapano, J. Roth, H. Zhang, L. Zhang, R. Haislmaier, R. Engel-Herbert, Frontiers in the growth of complex oxide thin films: Past, present, and future of hybrid MBE. *Adv. Funct. Mater.* **28**, 1702772 (2018).
13. J. L. MacManus-Driscoll, M. P. Wells, C. Yun, J.-W. Lee, C.-B. Eom, D. G. Schlom, New approaches for achieving more perfect transition metal oxide thin films. *APL Mater.* **8**, 040904 (2020).
14. S. Nair, Z. Yang, D. Lee, S. Guo, J. T. Sadowski, S. Johnson, A. Saboor, Y. Li, H. Zhou, R. B. Comes, W. Jin, K. A. Mkhoyan, A. Janotti, B. Jalan, Engineering metal oxidation using epitaxial strain. *Nat. Nanotechnol.* **18**, 1005–1011 (2023).
15. F. Gitmans, Z. Sitar, P. Günter, Growth of tantalum oxide and lithium tantalate thin films by molecular beam epitaxy. *Vacuum* **46**, 939–942 (1995).
16. Z. Sitar, F. Gitmans, W. Liu, P. Günter, Homo and heteroepitaxial growth of $LiTaO_3$ and $LiNbO_3$ by Mbe. *MRS Online Proc. Libr.* **401**, 255–260 (1995).
17. E. S. Hellman, E. H. Hartford, R. M. Fleming, Molecular beam epitaxy of superconducting $(Rb,Ba)BiO_3$. *Appl. Phys. Lett.* **55**, 2120–2122 (1989).
18. H.-M. Christen, D. P. Norton, L. A. Géa, L. A. Boatner, Pulsed laser deposition of solid-solution films using segmented targets. *Thin Solid Films* **312**, 156–159 (1998).
19. T. Schwaigert, S. Salmani-Rezaie, M. R. Barone, H. Paik, E. Ray, M. D. Williams, D. A. Muller, D. G. Schlom, K. Ahadi, Molecular beam epitaxy of $KTaO_3$. *J. Vac. Sci. Technol. A* **41**, 022703 (2023).
20. J. Chakhalian, X. Liu, G. A. Fiete, Strongly correlated and topological states in [111] grown transition metal oxide thin films and heterostructures. *APL Mater.* **8**, 050904 (2020).
21. I. Hallsteinsen, M. Nord, T. Bolstad, P.-E. Vullum, J. E. Boschker, P. Longo, R. Takahashi, R. Holmestad, M. Lippmaa, T. Tybell, Effect of polar (111)-oriented $SrTiO_3$ on initial perovskite growth. *Cryst. Growth Des.* **16**, 2357–2362 (2016).
22. J. Roth, T. Kuznetsova, L. Miao, A. Pogrebnyakov, N. Alem, R. Engel-Herbert, Self-regulated growth of [111]-oriented perovskite oxide films using hybrid molecular beam epitaxy. *APL Mater.* **9**, 021114 (2021).
23. Y. Liang, W. Li, S. Zhang, C. Lin, C. Li, Y. Yao, Y. Li, H. Yang, J. Guo, Homoepitaxial $SrTiO_3$ (111) film with high dielectric performance and atomically well-defined surface. *Sci. Rep.* **5**, 10634 (2015).
24. W. Huang, R. Nechache, S. Li, M. Chaker, F. Rosei, Electrical and optical properties of transparent conducting *p*-type $SrTiO_3$ thin films. *J. Am. Ceram. Soc.* **99**, 226–233 (2016).
25. M. Tyunina, J. Narkilahti, M. Plekh, R. Oja, R. M. Nieminen, A. Dejneka, V. Trepakov, Evidence for strain-induced ferroelectric order in epitaxial thin-film $KTaO_3$. *Phys. Rev. Lett.* **104**, 227601 (2010).
26. T. Esswein, N. A. Spaldin, Ferroelectric, quantum paraelectric, or paraelectric? Calculating the evolution from $BaTiO_3$ to $SrTiO_3$ to $KTaO_3$ using a single-particle quantum mechanical description of the ions. *Phys. Rev. Res.* **4**, 033020 (2022).
27. A. Gupta, H. Silotia, A. Kumari, M. Dumen, S. Goyal, R. Tomar, N. Wadehra, P. Ayyub, S. Chakraverty, $KTaO_3$—The new kid on the spintronics block. *Adv. Mater.* **34**, e2106481 (2022).
28. D. Maryenko, I. V. Maznichenko, S. Ostanin, M. Kawamura, K. S. Takahashi, M. Nakamura, V. K. Dugaev, E. Y. Sherman, A. Ernst, M. Kawasaki, Superconductivity at epitaxial $LaTiO_3$-$KTaO_3$ interfaces. *APL Mater.* **11**, 061102 (2023).
29. E. G. Arnault, A. H. Al-Tawhid, S. Salmani-Rezaie, D. A. Muller, D. P. Kumah, M. S. Bahramy, G. Finkelstein, K. Ahadi, Anisotropic superconductivity at $KTaO_3$ (111) interfaces. *Sci. Adv.* **9**, eadf1414 (2023).
30. S. Mallik, G. C. Ménard, G. Saïz, H. Witt, J. Lesueur, A. Gloter, L. Benfatto, M. Bibes, N. Bergeal, Superfluid stiffness of a $KTaO_3$-based two-dimensional electron gas. *Nat. Commun.* **13**, 4625 (2022).
31. C. Liu, X. Zhou, D. Hong, B. Fisher, H. Zheng, J. Pearson, J. S. Jiang, D. Jin, M. R. Norman, A. Bhattacharya, Tunable superconductivity and its origin at $KTaO_3$ interfaces. *Nat. Commun.* **14**, 951 (2023).
32. C. W. Rischau, X. Lin, C. P. Grams, D. Finck, S. Harms, J. Engelmayer, T. Lorenz, Y. Gallais, B. Fauqué, J. Hemberger, K. Behnia, A ferroelectric quantum phase transition inside the superconducting dome of $Sr_{1-x}Ca_xTiO_{3-\delta}$. *Nat. Phys.* **13**, 643–648 (2017).
33. S. Hameed, D. Pelc, Z. W. Anderson, A. Klein, R. J. Spieker, L. Yue, B. Das, J. Ramberger, M. Lukas, Y. Liu, M. J. Krogstad, R. Osborn, Y. Li, C. Leighton, R. M. Fernandes, M. Greven, Enhanced superconductivity and ferroelectric quantum criticality in plastically deformed strontium titanate. *Nat. Mater.* **21**, 54–61 (2022).
34. J. M. Edge, Y. Kedem, U. Aschauer, N. A. Spaldin, A. V. Balatsky, Quantum critical origin of the superconducting dome in $SrTiO_3$. *Phys. Rev. Lett.* **115**, 247002 (2015).
35. Y. Tokura, Quantum materials at the crossroads of strong correlation and topology. *Nat. Mater.* **21**, 971–973 (2022).
36. G. Yang, C. Ciccarelli, J. W. A. Robinson, Boosting spintronics with superconductivity. *APL Mater.* **9**, 050703 (2021).
37. K. M. Adkison, S.-L. Shang, B. J. Bocklund, D. Klimm, D. G. Schlom, Z.-K. Liu, Suitability of binary oxides for molecular-beam epitaxy source materials: A comprehensive thermodynamic analysis. *APL Mater.* **8**, 081110 (2020).
38. D. J. Baek, D. Lu, Y. Hikita, H. Y. Hwang, L. F. Kourkoutis, Ultrathin epitaxial barrier layer to avoid thermally induced phase transformation in oxide heterostructures. *ACS Appl. Mater. Inter.* **9**, 54–59 (2017).
39. See the Supplementary Materials.
40. B. Jalan, P. Moetakef, S. Stemmer, Molecular beam epitaxy of $SrTiO_3$ with a growth window. *Appl. Phys. Lett.* **95**, 032906 (2009).
41. A. Reisman, F. Holtzberg, M. Berkenblit, M. Berry, Reactions of the group VB pentoxides with alkali oxides and carbonates. III. Thermal and x-ray phase diagrams of the system $K_2O$ or $K_2CO_3$ with $Ta_2O_5$. *J. Am. Chem. Soc.* **78**, 4514–4520 (1956).
42. M. D. Biegalski, Y. Jia, D. G. Schlom, S. Trolier-McKinstry, S. K. Streiffer, V. Sherman, R. Uecker, P. Reiche, Relaxor ferroelectricity in strained epitaxial $SrTiO_3$ thin films on $DyScO_3$ substrates. *Appl. Phys. Lett.* **88**, 192907 (2006).
43. G. J. Omar, M. Li, X. Chi, Z. Huang, Z. S. Lim, S. Prakash, S. Zeng, C. Li, X. Yu, C. Tang, D. Song, A. Rusydi, T. Venkatesan, S. J. Pennycook, A. Ariando, Characteristic lengths of interlayer charge transfer in correlated oxide heterostructures. *Nano Lett.* **20**, 2493–2499 (2020).
44. Z. Chen, A. G. Swartz, H. Yoon, H. Inoue, T. A. Merz, D. Lu, Y. Xie, H. Yuan, Y. Hikita, S. Raghu, H. Y. Hwang, Carrier density and disorder tuned superconductor-metal transition in a two-dimensional electron system. *Nat. Commun.* **9**, 4008 (2018).
45. R. Uecker, B. Velickov, D. Klimm, R. Bertram, M. Bernhagen, M. Rabe, M. Albrecht, R. Fornari, D. G. Schlom, Properties of rare-earth scandate single crystals (Re=Nd−Dy). *J. Cryst. Growth* **310**, 2649–2658 (2008).
46. P. Modak, B. Modak, Energetic, electronic, and optical properties of intrinsic charge carrier-trapping defects in $KTaO_3$: Insights from a hybrid DFT study. *J. Phys. Chem. C* **125**, 24067–24078 (2021).
47. M. Setvin, M. Reticcioli, F. Poelzleitner, J. Hulva, M. Schmid, L. A. Boatner, C. Franchini, U. Diebold, Polarity compensation mechanisms on the perovskite surface $KTaO_3$ (001). *Science* **359**, 572–575 (2018).
48. N. Reyren, S. Thiel, A. D. Caviglia, L. F. Kourkoutis, G. Hammerl, C. Richter, C. W. Schneider, T. Kopp, A.-S. Ruetschi, D. Jaccard, M. Gabay, D. A. Muller, J.-M. Triscone, J. Mannhart, Superconducting interfaces between insulating oxides. *Science* **317**, 1196–1199 (2007).
49. Y. Li, C. Xiang, F. M. Chiabrera, S. Yun, H. Zhang, D. J. Kelly, R. T. Dahm, C. K. R. Kirchert, T. E. L. Cozannet, F. Trier, D. V. Christensen, T. J. Booth, S. B. Simonsen, S. Kadkhodazadeh, T. S. Jespersen, N. Pryds, Stacking and twisting of freestanding complex oxide thin films. *Adv. Mater.* **34**, e2203187 (2022).
50. H. Liu, H. Wu, K. P. Ong, T. Yang, P. Yang, P. K. Das, X. Chi, Y. Zhang, C. Diao, W. K. A. Wong, E. P. Chew, Y. F. Chen, C. K. I. Tan, A. Rusydi, M. B. H. Breese, D. J. Singh, L.-Q. Chen, S. J. Pennycook, K. Yao, Giant piezoelectricity in oxide thin films with nanopillar structure. *Science* **369**, 292–297 (2020).
51. Q. Xia, F. Zan, J. Xu, W. Liu, Q. Li, Y. He, J. Hua, J. Liu, Q. Zhang, J. Wang, C. Wu, H. Xia, All-solid-state thin film lithium/lithium-ion microbatteries for powering the internet of things. *Adv. Mater.* **35**, 2200538 (2023).
52. J. Levy, Correlated nanoelectronics and the second quantum revolution. *APL Mater.* **10**, 110901 (2022).
53. Scientific Group Thermodata Europe, *Thermodynamic Properties of Inorganic Materials* (Springer-Verlag, 1999).
54. A. Jain, S. P. Ong, G. Hautier, W. Chen, W. D. Richards, S. Dacek, S. Cholia, D. Gunter, D. Skinner, G. Ceder, K. A. Persson, Commentary: The Materials Project: A materials genome approach to accelerating materials innovation. *APL Mater.* **1**, 011002 (2013).
55. S. Kirklin, J. E. Saal, B. Meredig, A. Thompson, J. W. Doak, M. Aykol, S. Rühl, C. Wolverton, The Open Quantum Materials Database (OQMD): Assessing the accuracy of DFT formation energies. *NPJ Comput. Mater.* **1**, 15010 (2015).
56. J.-O. Andersson, T. Helander, L. Höglund, P. Shi, B. Sundman, Thermo-Calc & DICTRA, computational tools for materials science. *Calphad* **26**, 273–312 (2002).
57. G. L. Trigg, D. R. Lide, E. R. Cohen, *AIP Physics Desk Reference* (Springer, ed. 3, 2003).

**Acknowledgments**
**Funding:** Work at the University of Wisconsin was supported by the US Department of Energy (DOE), Office of Science, Basic Energy Sciences (BES) under award number DE-FG02-06ER46327

(C.-B.E.). Work at the University of Pittsburgh was supported by National Science Foundation (DMR-2225888) (J.L.), DOE-QIS program award number DE-SC0022277 (M.Y., R.R., and J.L.), and ONR MURI (N00014-21-1-2537) (J.L.). TEM work at Korea Institute of Energy Technology (KENTECH) was supported by the National Research Foundation of Korea (NRF) funded by the Korea government (MSIT) (No. NRF-2020R1A2C2101735), KENTECH Research Grant (KRG2022-01-019), andCenter for Shared Research Facilities. (S.H.O.). **Author contributions:** J.K., J.-W.L., and C.-B.E. conceived the project. C.-B.E., J.L., M.S.R., S.-Y.C., Z.-K.L., and S.H.O. supervised the project. J.K., J.-W.L., and K.E. fabricated and characterized the thin-film samples. S.-L.S. and Z.-K.L. carried out the thermodynamic calculations. J.S., G.-Y.K., S.-Y.C., and S.H.O. performed the STEM measurements. M.Y., P.P., and N.C. carried out the electrical transport measurements. M.Y. and R.R. carried out the magnetotransport and superconductivity measurements. J.K., M.Y., J.-W.L., S.-L.S., S.-Y.C., Z.-K.L., J.L., and C.-B.E. prepared the manuscript. C.-B.E. directed the overall research. **Competing interests:** J.K., J.-W.L., and C.-B.E. are co-inventors on a U.S. patent application based on the results of this work filed by the University of Wisconsin–Madison. All authors declare no other competing interests. **Data and materials availability:** All data needed to evaluate the conclusions in the paper are present in the paper and/or the Supplementary Materials.

Submitted 21 August 2023
Accepted 22 April 2024
Published 24 May 2024
10.1126/sciadv.adk4288